

Active Galactic Nucleus Pairs from the Sloan Digital Sky Survey. III. *Chandra* X-ray Observations Unveil Obscured Double Nuclei

MEICUN HOU,^{1,2,3} XIN LIU,^{3,4} HENGXIAO GUO,^{3,4} ZHIYUAN LI,^{1,2} YUE SHEN,^{3,4,*} AND PAUL J. GREEN⁵

¹*School of Astronomy and Space Science, Nanjing University, Nanjing 210046, China*

²*Key Laboratory of Modern Astronomy and Astrophysics (Nanjing University), Ministry of Education, Nanjing 210046, China*

³*Department of Astronomy, University of Illinois at Urbana-Champaign, Urbana, IL 61801, USA*

⁴*National Center for Supercomputing Applications, University of Illinois at Urbana-Champaign, 605 East Springfield Avenue, Champaign, IL 61820, USA*

⁵*Harvard-Smithsonian Center for Astrophysics, 60 Garden Street, Cambridge, MA 02138, USA*

ABSTRACT

We present *Chandra* ACIS-S X-ray imaging spectroscopy for five dual active galactic nucleus (AGN) candidates. Our targets were drawn from a sample of 1286 [O III]-selected AGN pairs systematically selected from the Sloan Digital Sky Survey Seventh Data Release. Each of the targets contains two nuclei separated by $\sim 3\text{--}9$ kpc in projection, both of which are optically classified as Type 2 (obscured) AGNs based on diagnostic ratios of the narrow emission lines. Combined with independent, empirical star formation rate estimates based on the host-galaxy stellar continua, the new *Chandra* X-ray observations allow us to evaluate the dual-AGN hypothesis for each merging system. We confirm two (SDSS J0907+5203 and SDSS J1544+0446) of the five targets as bona-fide dual AGNs. For the other three targets, the existing data are consistent with the dual-AGN scenario, but we cannot rule out the possibility of stellar/shock heating and/or one AGN ionizing both gaseous components in the merger. The average X-ray-to-[O III] luminosity ratio in our targets seems to be systematically smaller than that observed in single AGNs but is higher than that seen in dual AGNs selected from AGNs with double-peaked narrow emission lines. We suggest that the systematically smaller X-ray-to-[O III] luminosity ratio observed in dual AGNs than in single AGNs is due to a high nuclear gas column likely from strong merger-induced inflows. Unlike double-peaked-[O III]-selected dual AGNs, the new sample selected from resolved galaxy pairs are not subject to the orientation bias caused by the double-peak line-of-sight velocity splitting selection, which also contributes to lowering the X-ray-to-[O III] luminosity ratio.

Keywords: black hole physics – galaxies: active – galaxies: interactions – galaxies: nuclei – galaxies: Seyfert – X-rays: galaxies

1. INTRODUCTION

The observed growth of structures suggests that mergers of galaxies, and by extension, their central supermassive black holes (SMBHs; Kormendy & Richstone 1995; Ferrarese & Ford 2005), should be common throughout most of cosmic history. The final coalescence of merging SMBHs would produce low-frequency gravitational waves (GWs; e.g., Colpi & Dotti 2011), providing a “standard siren” for cosmology (Hughes 2009) and a direct testbed for strong-field General Relativity (Cen-

trella et al. 2010). Unlike LIGO’s stellar mass black holes (Abbott et al. 2016) whose detection is still limited to the relatively nearby universe, merging SMBHs would be detectable close to the edge of the observable universe (Cornish & Robson 2018). They are being hunted currently by pulsar timing arrays for the more massive, low-redshift population (e.g., Arzoumanian et al. 2018), and in the future by space-borne experiments for the less massive, high-redshift population (e.g., Amaro-Seoane et al. 2017).

While the GWs from merging SMBHs are yet to be detected, it is useful to study their progenitors – pairs of SMBHs selected by their electromagnetic signatures from accreting materials from the surroundings. These

houmc@smail.nju.edu.cn, xinliuxl@illinois.edu

* Alfred P. Sloan Research Fellow

so-called “dual active galactic nuclei (AGNs)” are AGN pairs in merging galaxies with typical separations of a few kiloparsecs (Gerke et al. 2007; Comerford et al. 2009; Xu & Komossa 2009). Dual AGNs and AGN pairs in general provide an exciting prospect for understanding massive black hole growth and their merger rates in galaxies in the era of multi-messenger astronomy (e.g., Bhowmick et al. 2019). The first concrete evidence for dual AGNs was a serendipitous discovery by *Chandra* in NGC 6240 (Komossa et al. 2003), a $z = 0.02$ merging ultra-luminous infrared galaxy (ULIRG), which contains two X-ray nuclei separated by $\sim 1''$ (~ 0.7 kpc) in projection. Until recently only a handful of other secure cases were known in the X-rays (e.g., 3C 75 (Hudson et al. 2006), Mrk 463 (Bianchi et al. 2008; Treister et al. 2018), Mrk 266 (Brassington et al. 2007; Mazzarella et al. 2012), and Mrk 739 (Koss et al. 2011); but see also Arp 299 (Ballo et al. 2004) for a candidate), all of which were confirmed by *Chandra*.

The past decade has seen significant progress in finding concrete evidence for dual AGNs at $z < 0.5$ thanks to systematic searches using large surveys combined with dedicated follow ups, in particular in the X-rays, mid-IR, and radio (e.g., Green et al. 2010; Fabbiano et al. 2011; Liu et al. 2013; Comerford et al. 2015; Kocevski et al. 2015; Fu et al. 2015; Gatti et al. 2016; Koss et al. 2016; Satyapal et al. 2017; Ellison et al. 2017; Fu et al. 2018; De Rosa et al. 2018; Liu et al. 2018; Vignali et al. 2018; Pfeifle et al. 2019). Liu et al. (2011) identified a sample of 1286 [O III]-selected, spatially resolved AGN pairs from the Sloan Digital Sky Survey (SDSS) Seventh Data Release (DR7; Abazajian et al. 2009). Among the 1286 pairs, 94 have projected nuclear separation $r_p < 10$ kpc, making them the largest sample of [O III]-selected dual AGN candidates. Each of these galaxies contains two nuclei separated by a few arcsec, both of which have individual SDSS spectra. Due to the finite size of SDSS fibers (i.e., fiber collisions), two objects separated by $< 55''$ cannot both be spectroscopically observed unless being on overlapping plates. We have corrected for this spectroscopic incompleteness when calculating the frequency of dual AGNs (Liu et al. 2011). Based on the SDSS spectra, both nuclei in the candidates are optically classified as Type 2 (i.e., obscured) AGNs according to diagnostic ionization ratios of narrow emission lines (Baldwin et al. 1981; Veilleux & Osterbrock 1987; Kewley et al. 2001). However, optical diagnostic line ratios only represent indirect evidence for dual AGNs; they cannot conclusively rule out alternative scenarios for the nature of the ionizing sources such as stellar/shock heating, and/or a pair of merging galaxy components ionized by a single active nucleus.

It is generally thought that the X-ray band can provide more direct evidence for nuclear activity. In particular, hard X-rays (defined here as 2-10 keV) are transparent to column densities of $N_H \lesssim 10^{24}$ cm $^{-2}$, while Compton-thick AGNs can be revealed at energies $\gtrsim 10$ keV (LaMassa et al. 2011; Lansbury et al. 2015; Nardini 2017).

We here present a new *Chandra* ACIS-S X-ray imaging of five dual AGN candidates drawn from the parent sample of 94 closely separated, dual AGN candidates (Figure 1). Figure 2 shows their optical and X-ray images. *Chandra*’s high image quality (FWHM $\lesssim 1''$) and its capability of moderate spectral resolution imaging spectroscopy in the X-rays make it ideal for assessing the dual-AGN hypothesis. Unlike previous *Chandra*’s searches for dual AGNs in galaxy pairs hosting single AGNs (e.g., Teng et al. 2012), we target merging galaxies where *both* nuclei are [O III]-selected AGNs.

The paper is organized as follows. Section 2 describes the target selection and their optical properties. Section 3 presents the new *Chandra* ACIS-S X-ray observations, data reduction, and data analysis. Section 4 shows the results on the X-ray luminosities and spectral properties, the X-ray contribution from star formation, and the nature of the nuclear ionizing sources. Finally, we discuss the implications of our results in Section 5 and summarize the main conclusions in Section 6. Throughout this paper, we assume a concordance cosmology with $\Omega_m = 0.3$, $\Omega_\Lambda = 0.7$, and $H_0 = 70$ km s $^{-1}$ Mpc $^{-1}$, and use the AB magnitude system (Oke 1974).

2. TARGET SELECTION AND OPTICAL PROPERTIES

Our targets are drawn from a parent sample of 1286 spectroscopic AGN pairs with $r_p < 100$ kpc and line-of-sight velocity offsets < 600 km s $^{-1}$ selected from a heterogeneous sample of 138,070 optical AGNs from the SDSS DR7. The optical AGN sample consists of 129,277 Type 2 (i.e., narrow-line) AGNs, 5,564 Type 1 (i.e., broad-line) AGNs, 3,117 Type 1 quasars, and 112 Type 2 quasars (Liu et al. 2011). The parent AGN pair sample is dominated by Type 2 AGNs whose optical narrow emission-line ratios are characteristic of Seyferts, LINERs, and/or AGN-H II composites.

From the parent AGN pair sample, we select kpc-scale dual AGN candidates by first requiring $r_p < 10$ kpc. We further select systems in which both nuclei have high enough [O III] fluxes to expect at least 50 hard (2-10 keV) X-ray counts in 15 ks for the weaker component (see details below). We additionally exclude systems with existing *Chandra* observations to avoid duplicate observations (e.g., Mrk 266). For systems with simi-

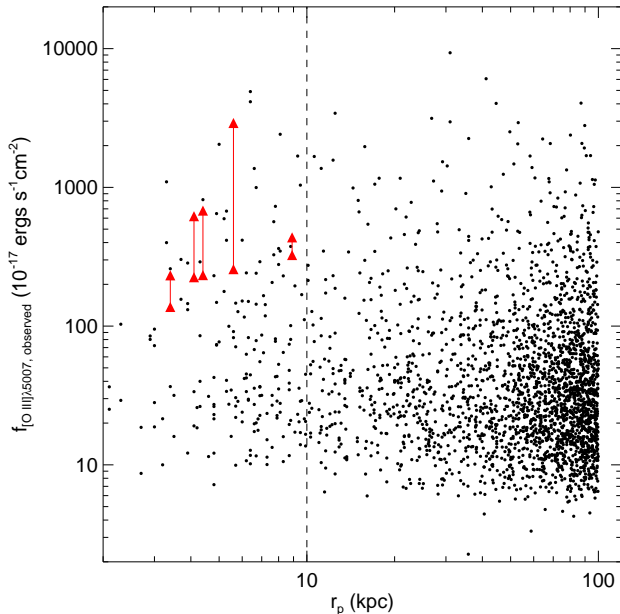


Figure 1. [O III] flux vs. projected separation r_p for our five target pairs and parent sample of 1286 AGN pairs (Liu et al. 2011) in red triangles and black dots, respectively. Our five targets are selected by requiring $r_p < 10$ kpc and both nuclei have sufficiently high [O III] fluxes. The vertical dashed line marks the position of $r_p = 10$ kpc.

lar [O III] fluxes, targets which are classified as Seyferts based on the BPT diagram are prioritized over those that are classified as AGN-H II composites to maximize the probability of X-ray detections. Therefore, our final target sample consists of five dual AGN candidates. The distribution of our sample is shown in Figure 1. Tables 1 and 2 list their basic photometric and spectroscopic properties. The stellar velocity dispersion was measured by fitting the host-galaxy stellar continuum using the penalized Pixel-Fitting (pPXF) method (Cappellari & Emsellem 2004) (see the Appendix for details). The total stellar mass was given by the MPA-JHU DR7 catalog from fitting the photometry (Kauffmann et al. 2003a; Salim et al. 2007). Figure 3 shows the narrow emission-line ratios measured from the SDSS spectra subtracted for stellar continua using the pPXF fits. It illustrates that the nuclei in our targets are optically classified as Type 2 Seyferts, LINERs, or AGN-H II composites.

3. OBSERVATIONS, DATA REDUCTION, AND DATA ANALYSIS

3.1. Chandra ACIS X-ray Imaging Spectroscopy

We observed the five dual-AGN candidates with the ACIS-S on board the *Chandra* X-ray Observatory between 2012 December and 2013 April (Program GO-14700264, PI: X. Liu). All targets were observed on-axis on the S3 chip, $5.2''$ to $15.0''$ away from the aimpoint.

Each target was observed for 15 ks (Table 3). The exposure time was set to obtain ~ 50 counts in the 2–10 keV range from the [O III] weaker nucleus in each merger, although the estimate was too optimistic. We estimated the X-ray counts from the [O III] luminosity for each nucleus (corrected for [O III] emission due to star formation in AGN-H II composites (Kauffmann & Heckman 2009)), assuming an empirical correlation between the 2–10 keV (unabsorbed) and [O III] luminosities. Measurements of $L_{2-10\text{ keV}}/L_{[\text{O III}]}$ for optically selected Type 2 AGNs span a wide range (Mulchaey et al. 1994; Heckman et al. 2005; Panessa et al. 2006), with values from a few to a few hundred. For the baseline assumption, we adopted the mean calibration of Panessa et al. (2006) given by,

$$\log \left[\frac{L_{2-10\text{ keV}}}{\text{erg s}^{-1}} \right] = (1.22 \pm 0.06) \log \left[\frac{L_{[\text{O III}]}}{\text{erg s}^{-1}} \right] + (-7.34 \pm 2.53), \quad (1)$$

where the [O III] luminosities have been corrected for the Galactic and intrinsic NLR extinction by using the Balmer decrement method via $H\alpha/H\beta$ ratio. We accounted for systematic uncertainties using the Heckman et al. (2005) relation based on optically selected (single) Type 2 AGNs. An X-ray power-law spectrum was assumed with an absorbing column density $N_{\text{H}} = 10^{22} \text{ cm}^{-2}$ (typical for our targets for which enough counts were detected for spectral analysis (see below) and for Type 2 Seyferts; Bassani et al. 1999) and a photon index $\Gamma = 1.7$ (typical for unabsorbed Seyferts; Green et al. 2009).

We reprocessed the data using CIAO v4.8 and the corresponding calibration files following standard procedure¹. We examined the light curve of each observation and found no time interval of high background. We produced counts and exposure maps with the original pixel scale ($0''.492 \text{ pixel}^{-1}$) in the 0.5–2 keV (*S*), 2–8 keV (*H*), and 0.5–8 keV (*F*) bands. The exposure maps were weighted by the above fiducial incident spectrum.

Following the source detection procedure detailed in Wang (2004) and Hou et al. (2017), we detect X-ray sources in the *S*, *H* and *F* bands in each image. With a local false detection probability $P \leq 10^{-6}$ (empirically yielding ~ 0.1 false detection per field), we detected a total of 124 sources in the field-of-view covered by the S3 and S2 CCDs. For each detected source, we derived background-subtracted and exposure map-corrected count rates in each individual band from within the 90% enclosed-energy radius (EER), taking into account the position-dependent point-spread function and the local background.

¹ <http://cxc.harvard.edu/ciao/>

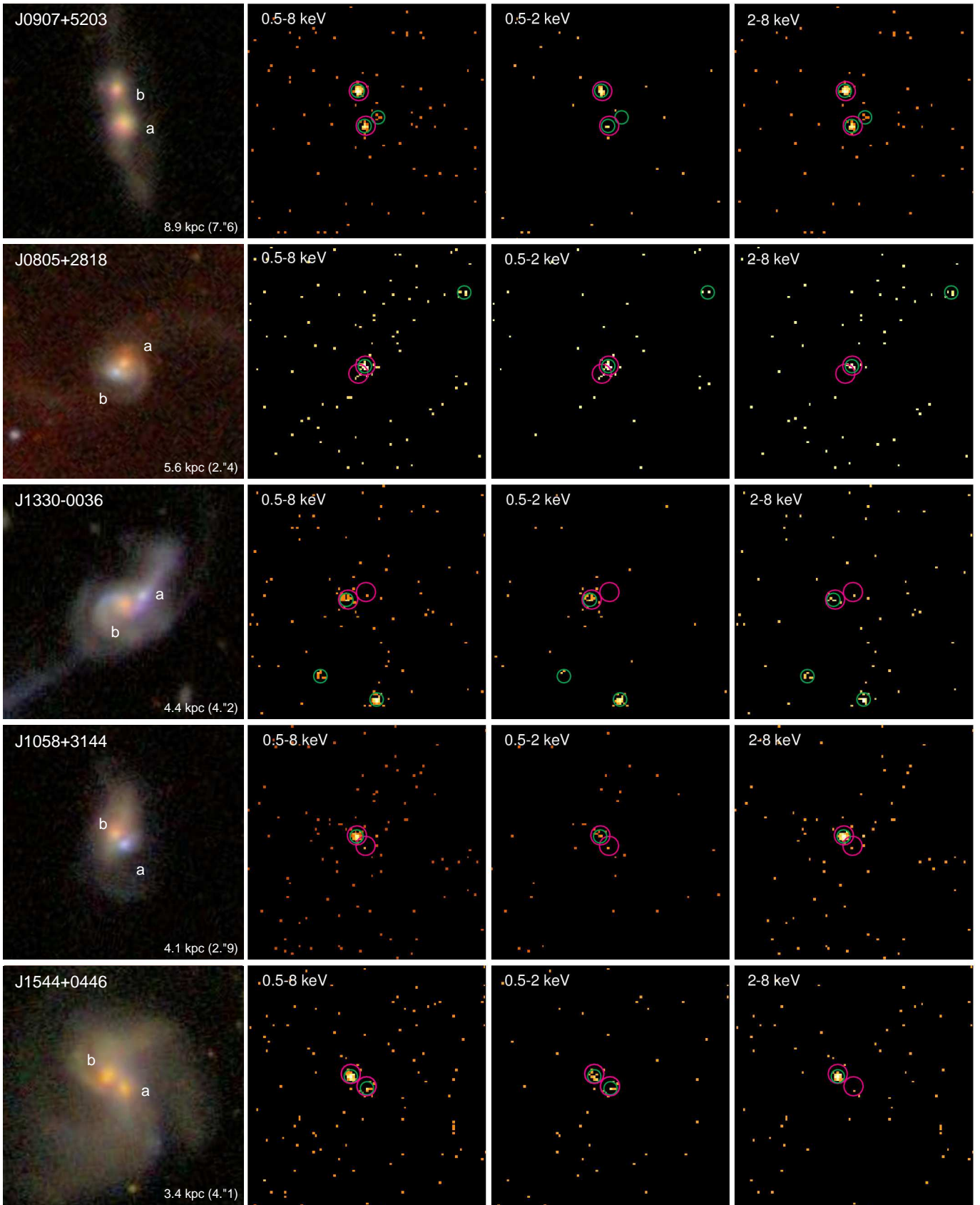


Figure 2. SDSS *gri*-color composite, *Chandra* 0.5–8 keV, 0.5–2 keV, and 2–8 keV images of the five [O III]-selected dual-AGN candidates. Each panel is $50'' \times 50''$. North is up and east is to the left. The targets are ordered with decreasing projected separation (as labeled, with angular distance in parenthesis) from top to bottom. Magenta circles denote positions of the optical nuclei whereas green circles represent the 90% EER of the detected X-ray sources. Table 1 lists their basic properties.

Table 1. [O III]-Selected Dual AGN Candidates with New *Chandra* ACIS-S X-ray Observations.

Full Name	Name	Redshift	r_p	Plate	Fiber ID	MJD	m_r	σ_*	$\log M_{\text{BH}}$	$\log M_*$
(1)	(2)	(3)	(4)	(5)	(6)	(7)	(8)	(9)	(10)	(11)
J090714.45+520343.4	J0907+5203a	0.0596	8.9	553	208	51999	16.27	177	7.9	10.6
J090714.61+520350.7	J0907+5203b	0.0602	8.9	552	603	51992	16.95	132	7.4	10.3
J080523.29+281815.8	J0805+2818a	0.1284	5.6	929	570	52581	15.99	316	9.0	11.2
J080523.40+281814.1	J0805+2818b	0.1286	5.6	930	285	52618	18.18	169	7.8	9.8
J133031.75−003611.9	J1330−0036a	0.0542	4.4	298	264	51955	18.36	72	6.2	8.8
J133032.00−003613.5	J1330−0036b	0.0542	4.4	297	61	51959	15.17	153	7.6	10.7
J105842.44+314457.6	J1058+3144a	0.0728	4.1	1990	342	53472	17.27	101	6.9	10.0
J105842.58+314459.8	J1058+3144b	0.0723	4.1	2026	17	53711	15.79	159	7.7	10.9
J154403.45+044607.5	J1544+0446a	0.0420	3.4	2950	278	54559	17.82	153	7.6	9.8
J154403.67+044610.1	J1544+0446b	0.0416	3.4	1836	586	54567	14.21	201	8.1	11.1

NOTE—(1) SDSS names with J2000 coordinates given in the form of “hhmmss.ss+ddmmss.s”; (2) Abbreviated Name, a and b for each dual AGN candidate are ordered with R.A.; (3) Spectroscopic redshift from the SDSS DR7; (4) Projected physical separation of dual AGN in each pair, in units of kpc; (5)-(7) SDSS spectroscopic plate number, fiber ID, and Modified Julian Date; (8) SDSS r-band model magnitude; (9) Stellar velocity dispersion provided in the MPA-JHU DR7 catalog, in units of km s^{-1} ; (10) Black hole mass estimate inferred from σ_* assuming the $M_{\text{BH}}-\sigma_*$ relation of Gültekin et al. (2009), in units of M_\odot ; (11) Total stellar mass from fits to the photometry provided in the MPA-JHU DR7 catalog (Salim et al. 2007), in units of M_\odot .

Table 2. Optical Emission-line Properties of the Five [O III]-Selected Dual AGN Candidates.

Name	H β	H α	[O III]	[N II]	[S II]	[O I]	$\frac{[\text{O III}]}{\text{H}\beta}$	$\frac{[\text{N II}]}{\text{H}\alpha}$	$\frac{[\text{S II}]}{\text{H}\alpha}$	$\frac{[\text{O I}]}{\text{H}\alpha}$
(1)	(2)	(3)	(4)	(5)	(6)	(7)	(8)	(9)	(10)	(11)
J0907+5203a	98.8 ± 70.9	361.6 ± 81.5	632.4 ± 141.8	213.0 ± 81.5	172.8 ± 80.2	69.1 ± 67.4	6.4 ± 4.8	0.6 ± 0.3	0.5 ± 0.2	0.2 ± 0.2
J0907+5203b	130.9 ± 29.9	581.7 ± 40.6	492.3 ± 49.1	348.1 ± 36.3	296.2 ± 33.2	98.0 ± 25.6	3.8 ± 0.9	0.6 ± 0.1	0.5 ± 0.1	0.2 ± 0.0
J0805+2818a	390.0 ± 102.2	1578.6 ± 180.2	3808.5 ± 266.3	1023.7 ± 161.4	554.2 ± 135.7	249.4 ± 72.6	9.8 ± 2.6	0.6 ± 0.1	0.4 ± 0.1	0.2 ± 0.0
J0805+2818b	52.7 ± 43.0	150.4 ± 40.2	360.1 ± 103.3	201.1 ± 60.3	74.6 ± 70.1	29.3 ± 40.2	6.8 ± 5.9	1.3 ± 0.5	0.5 ± 0.5	0.2 ± 0.3
J1330−0036a	111.6 ± 8.2	398.8 ± 49.3	264.2 ± 12.2	182.0 ± 10.2	146.1 ± 56.9	28.5 ± 46.9	2.4 ± 0.2	0.5 ± 0.1	0.4 ± 0.1	0.1 ± 0.1
J1330−0036b	367.6 ± 144.1	1568.2 ± 227.7	1120.1 ± 251.0	1426.4 ± 218.5	539.2 ± 151.3	110.7 ± 106.9	3.0 ± 1.4	0.9 ± 0.2	0.3 ± 0.1	0.1 ± 0.1
J1058+3144a	129.7 ± 15.3	377.3 ± 50.1	228.2 ± 30.0	239.2 ± 20.8	132.9 ± 51.0	25.9 ± 38.8	1.8 ± 0.3	0.6 ± 0.1	0.4 ± 0.1	0.1 ± 0.1
J1058+3144b	238.7 ± 83.8	921.0 ± 127.2	759.7 ± 145.9	762.2 ± 117.9	316.4 ± 85.6	64.2 ± 62.1	3.2 ± 1.3	0.8 ± 0.2	0.3 ± 0.1	0.1 ± 0.1
J1544+0446a	46.1 ± 38.5	209.1 ± 40.6	153.7 ± 57.7	613.8 ± 68.4	238.2 ± 54.4	97.9 ± 44.9	3.3 ± 3.1	2.9 ± 0.7	1.1 ± 0.3	0.5 ± 0.2
J1544+0446b	165.8 ± 62.6	749.4 ± 122.0	285.9 ± 85.7	643.3 ± 105.5	364.2 ± 86.3	105.7 ± 65.9	1.7 ± 0.8	0.9 ± 0.2	0.5 ± 0.1	0.1 ± 0.1

NOTE—(2)-(7) Optical emission-line fluxes and 1σ uncertainties in units of $10^{-17} \text{ erg s}^{-1} \text{ cm}^{-2}$; (8)-(11) Optical diagnostic emission-line ratios and 1σ uncertainties estimated from error propagation.

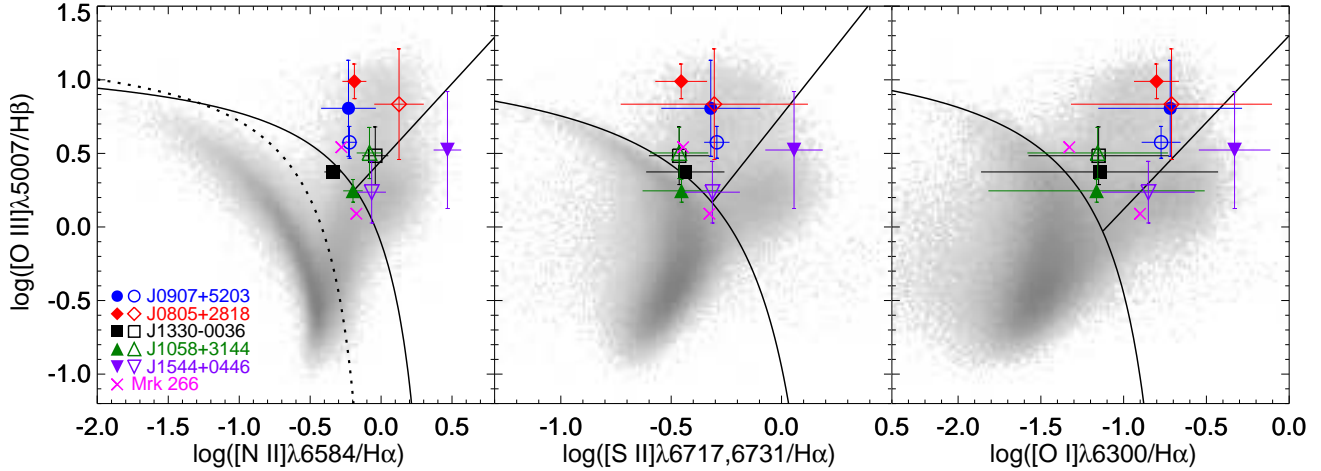


Figure 3. Optical diagnostic emission-line ratios (Baldwin et al. 1981; Veilleux & Osterbrock 1987) of the 10 nuclei in our five dual AGN candidates (colored solid symbols) and of the two nuclei in Mrk 266 (red crosses). Gray scales indicate number densities of SDSS DR4 emission-line galaxies (Kauffmann et al. 2003b). The dashed curve denotes the empirical separation between H II regions and AGNs (Kauffmann et al. 2003b), the solid curve displays the theoretical “starburst limit” (Kewley et al. 2001), and the solid line represents the empirical division between Seyferts and LINERs (Kewley et al. 2006). Pure star-forming (“SF”) galaxies lie below the dashed curve, AGN-dominated objects (Seyferts above and LINERs below the solid line) lie above the solid curve, and AGN-H II composites lie in between.

Table 3. *Chandra* Observations of the Five [O III]-Selected Dual AGN Targets.

Name	ObsID	Exp.	Counts	CR	CR1	CR2	HR	Γ	N_{H}
(1)	(2)	(3)	(4)	(5)	(6)	(7)	(8)	(9)	(10)
J0907+5203a	14965	14.5	33.9	2.76 ± 0.44	0.33 ± 0.15	2.43 ± 0.42	$0.76^{+0.12}_{-0.10}$	-	-
J0907+5203b*	14965	14.5	108.9	7.63 ± 0.73	1.57 ± 0.32	6.06 ± 0.66	$0.56^{+0.08}_{-0.07}$	$1.43^{+0.84}_{-0.75}$	$2.6^{+1.5}_{-1.1}$
J0805+2818a	14964	14.0	28.9	2.04 ± 0.38	1.16 ± 0.28	0.89 ± 0.26	$-0.17^{+0.18}_{-0.19}$	-	-
J0805+2818b	14964	14.0	< 12.4	< 0.87	< 0.88	< 0.45	-	-	-
J1330-0036a	14967	14.9	< 8.4	< 0.57	< 0.43	< 0.59	-	-	-
J1330-0036b	14967	14.9	15.9	1.05 ± 0.27	0.57 ± 0.19	0.48 ± 0.18	$-0.13^{+0.27}_{-0.28}$	-	-
J1058+3144a	14966	14.5	< 12.1	< 0.81	< 0.72	< 0.57	-	-	-
J1058+3144b*	14966	14.5	79.8	5.99 ± 0.66	0.26 ± 0.13	5.73 ± 0.64	$0.91^{+0.05}_{-0.04}$	$1.13^{+1.64}_{-1.50}$	$6.4^{+6.3}_{-4.5}$
J1544+0446a	14968	14.9	5.8	0.38 ± 0.16	0.32 ± 0.14	< 0.58	$-0.62^{+0.09}_{-0.38}$	-	-
J1544+0446b*	14968	14.9	49.9	3.93 ± 0.52	0.45 ± 0.17	3.48 ± 0.49	$0.76^{+0.10}_{-0.08}$	$1.66^{+1.47}_{-1.35}$	$3.9^{+3.2}_{-2.7}$

NOTE—* represent the targets with sufficient net counts for spectral analysis (see Section 3.2). (2) *Chandra* observation ID; (3) *Chandra* effective exposure, in units of ks; (4) Observed net counts in 0.5-8 keV band; (5)-(7) Observed count rate in 0.5-8 (*F*), 0.5-2 (*S*) and 2-8 (*H*) keV bands, in units of 10^{-3} counts s^{-1} ; (8) Hardness ratio, defined as $HR = (H - S)/(H + S)$; (9) Best-fitted photon index of a power-law model; (10) Best-fitted intrinsic column density of a power-law model, in units of 10^{22} cm^{-2} .

Figure 2 shows the ACIS images of the five targets in the *F*, *S* and *H* bands. Table 3 summarizes the X-ray measurements. Given the low count levels, we do not apply any smoothing to avoid artifacts. As we will show in Section 4.1, our targets are significantly weaker hard X-ray emitters than those predicted from both the Panessa et al. (2006) and Heckman et al. (2005) relations based on single optically selected AGNs, resulting in far fewer counts than expected. Seven of the ten nuclei in

our targets were detected in the *F*-band. Six nuclei were detected in both *S* and *H* bands, whereas one nucleus (J1544+0446a) was detected in the *S* band only. Three nuclei (J0805+2818b, J1330-0036a and J1058+3144a) were undetected in the X-rays.

3.2. Spectral Analysis and Hardness Ratio

Three of the seven X-ray detected nuclei have sufficient net counts (≥ 50) for spectral analysis. For these nuclei, we extracted spectra from within the 90% EER of

each source of interest using the CIAO tool *specextract* and built the Response Matrix Files (RMFs) and Ancillary Response Files (ARFs); the corresponding background spectrum was extracted typically between two to five times the 90% EER. For nucleus J1544+0446b, with the other X-ray detected nucleus located in the background extraction region given the small projected nuclear separation ($4.1''$), we further removed the 90% EER of this other nucleus from the background to eliminate its contamination. We fit each spectrum with an absorbed power-law model. Due to the low net counts, we adopted the C-statistic (a Poisson log-likelihood function, taking into account the known Poisson background, *pstat* in XSpec) for the spectral fitting (Cash 1979). Figure 4 shows the fitted spectra. Table 3 lists the spectral fitting results. The best-fit power-law spectral index and the absorption column density are consistent with Type-2 AGN for all three nuclei.

For the other four X-ray detected AGNs with < 50 net counts, we estimate their spectral properties using hardness ratios (HR). The hardness ratio is defined as

$$\text{HR} \equiv \frac{H - S}{H + S}, \quad (2)$$

where H and S are the number of counts in the hard and soft X-ray bands, respectively. We adopt the Bayesian Estimation of Hardness Ratios (BEHR; Park et al. 2006) to measure the HRs and their uncertainties, which is appropriate for the low count regime. Table 3 lists the HR results.

For the three sources without X-ray detection and one nucleus (J1544+0446a) without X-ray detection in H band, we estimate the X-ray net counts 3σ upper limit using the CIAO tool *aprate*.

4. RESULTS

4.1. X-ray Luminosities

X-ray emission provides the most direct evidence for nuclear activity. The 2–10 keV hard X-ray band is transparent to column densities of $N_{\text{H}} \lesssim 10^{24} \text{ cm}^{-2}$. To infer X-ray luminosity, we assume a simple absorbed power-law model. For the three nuclei with enough counts for X-ray spectral analysis, we adopt the best-fit column density and photon index given in Table 3. For the other seven nuclei without enough counts or without X-ray detection, we assume a photon index of 1.7 and an absorption column density $N_{\text{H}} = 10^{22} \text{ cm}^{-2}$. In Table 4 we list the unabsorbed/intrinsic X-ray luminosity or upper limit of each nucleus in the total, soft, and hard bands, respectively.

The adopted single absorbed power-law model is most likely too simple for the X-ray spectra of obscured

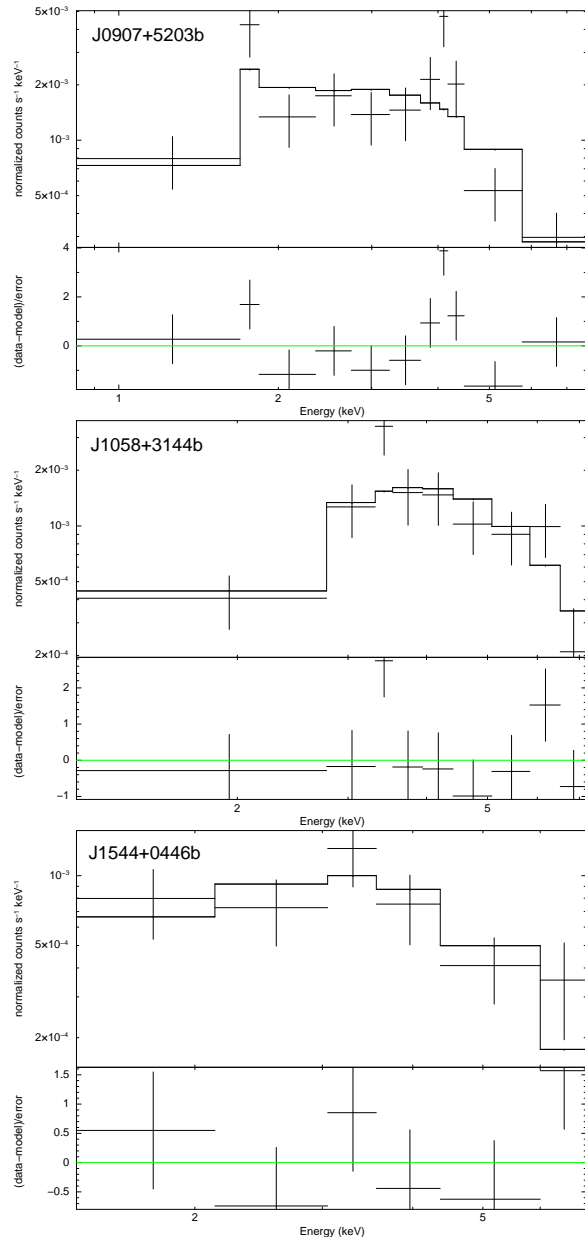


Figure 4. Spectra modeling for three X-ray detected nuclei with > 50 net counts. The spectra have been grouped to achieved a signal-to-noise ratio of 3. The fitted model is an absorbed power law. The best-fit photon index and intrinsic column density are listed in Table 3. For each nucleus the lower panel shows the sigma of residuals.

AGNs, in which thermal emission from starburst components and/or scattered nuclear emission are often present (e.g., Turner et al. 1997a,b). However, the low counts of our detections do not allow us to test more realistic models. In addition, our estimates of the intrinsic absorbing column may not necessarily reflect the true values in cases of patchy obscuration and/or significant scattering off of an ionized medium in Compton-thick

(i.e., $N_{\text{H}} \sim 10^{24} \text{ cm}^{-2}$ or larger) AGNs [which represent about half of the local Type 2 Seyfert population (Risaliti et al. 1999)], as observed in NGC 6240 (e.g., Vignati et al. 1999; Ptak et al. 2003) and in NGC 1068 (e.g., Matt et al. 1997; Guainazzi et al. 1999), although, again, the quality of our data do not allow us to robustly test these possibilities.

The seven X-ray detected nuclei have estimated unabsorbed 0.5–8 keV luminosities ranging from $3.1 \times 10^{40} \text{ erg s}^{-1}$ to $4.1 \times 10^{42} \text{ erg s}^{-1}$. One nucleus J1544+0446a is not detected in the hard band, and the remaining six hard X-ray detected nuclei have estimated unabsorbed 2–10 keV luminosities ranging from $9.0 \times 10^{40} \text{ erg s}^{-1}$ to $4.0 \times 10^{42} \text{ erg s}^{-1}$. Figure 5 shows the comparison of [O III] luminosities (both observed and extinction-corrected) and 2–10 keV X-ray luminosities (both observed and unabsorbed). The estimated upper limits for the four hard X-ray undetected nuclei range from $6.5 \times 10^{40} \text{ erg s}^{-1}$ to $5.1 \times 10^{41} \text{ erg s}^{-1}$ in 2–10 keV. These luminosity estimates are comparable to or smaller than those of the previously known X-ray confirmed dual AGNs (e.g., Komossa et al. 2003; Ballo et al. 2004; Hudson et al. 2006; Bianchi et al. 2008; Mazzarella et al. 2012; Koss et al. 2011).

4.2. X-ray Contribution from Nuclear Starburst

The estimated intrinsic hard X-ray luminosities of our targets are close to or below $\sim 10^{42} \text{ ergs s}^{-1}$ – the characteristic upper limit for the most luminous star-forming galaxies (e.g., Zezas et al. 2001). Hence it is possible that much or all of the luminosity is due to star formation. X-ray spectral shape offers another diagnostic to discriminate between AGN and starburst scenarios. However, the uncertainties of our spectral estimates are too large to draw firm conclusions for the majority of the nuclei.

We use independent star formation rate (SFR) estimates to test the AGN scenario for each nucleus. To estimate the expected X-ray emission due to star formation within similar apertures used to perform our X-ray extraction (typically a radius of $2''$), we use the SDSS fiber SFR given by the MPA-JHU DR7 catalog (Salim et al. 2007). For galaxies classified as AGNs or composites according to the optical BTP diagram, which are the case for our targets, the SFRs are estimated by constructing the likelihood distribution of the specific SFR as a function of the 4000 Å break $D_n(4000)$ based on the star-forming sample (Brinchmann et al. 2004) multiplied by the stellar mass.

To derive X-ray luminosities from the fiber SFRs, we adopt the empirical calibration of Ranalli et al. (2003, see also Grimm et al. 2003) based on 23 nearby star-

forming galaxies, which is given by

$$L_{0.5-2 \text{ keV}}^{\text{SF}} = 4.5 \times 10^{39} \frac{\text{SFR}}{M_{\odot} \text{ yr}^{-1}} \text{ erg s}^{-1}, \quad (3)$$

$$L_{2-10 \text{ keV}}^{\text{SF}} = 5.0 \times 10^{39} \frac{\text{SFR}}{M_{\odot} \text{ yr}^{-1}} \text{ erg s}^{-1}, \quad (4)$$

with an rms scatter of 0.27 dex and 0.29 dex. In Table 4 we list the fiber SFR estimates and the derived $L_{0.5-2 \text{ keV}}^{\text{SF}}$ and $L_{2-10 \text{ keV}}^{\text{SF}}$ estimates for each nucleus. Figure 6 compares the expected X-ray luminosities due to star formation against the observed X-ray luminosities in the soft and hard bands. In both bands, the predicted X-ray contribution from star formation for the majority of our targets' nuclei is below the observed X-ray luminosity, suggesting an additional excitation source from the AGN. We caution, however, that there are significant systematic uncertainties of our estimates of the expected X-ray luminosities due to star-formation-related processes (e.g., uncertainties in the IMF, extinction correction; Liu et al. 2013).

We also test the contribution to hard X-ray luminosity from low-mass X-ray binaries, which is proportional to stellar mass (M_*). Based on the $L_X - M_*$ relations from Gilfanov (2004) or Lehmer et al. (2010), the estimated contribution from stellar mass enclosed in the SDSS fiber is negligible compared to the contribution from star forming activity (typically $< 10\%$ and never exceeding 30%).

4.3. Results on Individual Targets

4.3.1. SDSS J0907+5203

Both galaxies in the merger are optically classified as Type 2 Seyferts (Figure 3). Both nuclei were detected in both soft and hard X-ray bands. The northern galaxy (J0907+5203b) has enough counts for X-ray spectral analysis, which suggests moderate nuclear obscuration, with an estimated column density of $N_{\text{H}} \approx 2.6_{-1.1}^{+1.5} \times 10^{22} \text{ cm}^{-2}$. The spatial profiles of the two nuclear X-ray sources are consistent with the AGN scenarios for both galaxies. For both galaxies, the expected star-formation-induced X-ray luminosities are too low to explain the observed values in both soft and hard X-ray bands (Figure 6), consistent with the dual AGN scenario.

4.3.2. SDSS J0805+2818

The NW nucleus (J0805+2818a) in the merger is optically classified as a Type 2 Seyfert whereas the SE nucleus (J0805+2818b) a Type 2 Seyfert or a LINER (Figure 3). Only the NW nucleus was detected in both soft and hard X-ray bands; the SE nucleus was detected in neither. The host galaxy of the SE nucleus shows

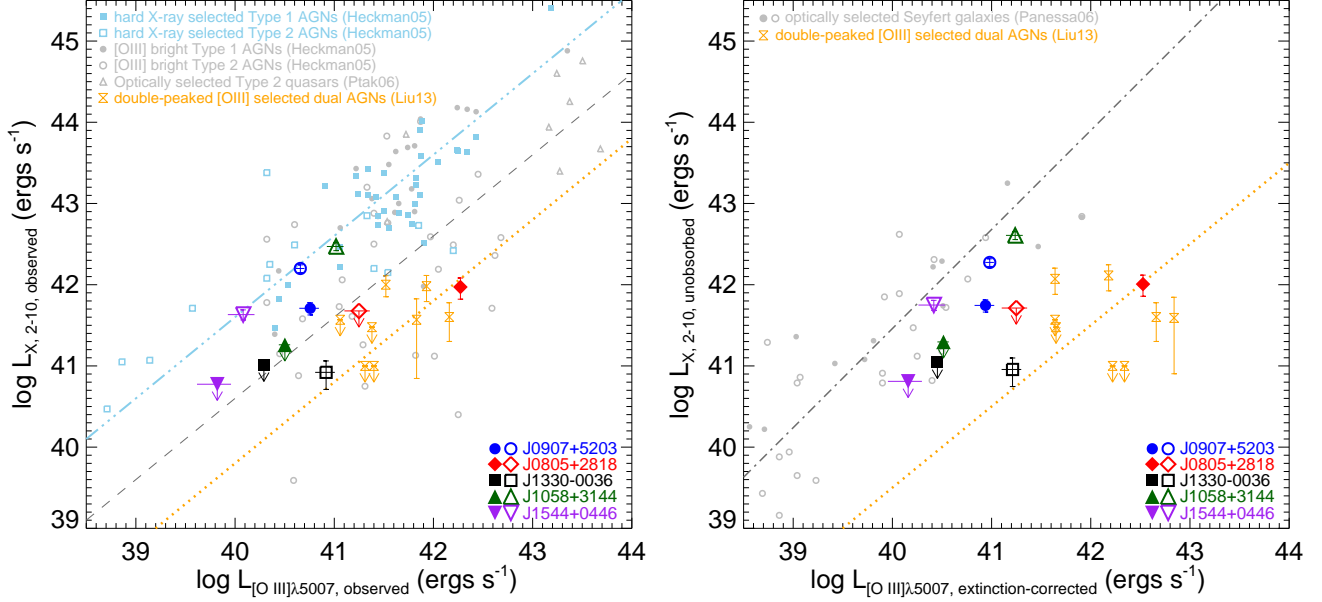


Figure 5. Hard X-ray luminosities vs. [O III] luminosities. Left panel: observed 2-10 keV luminosity vs. observed [O III] luminosity. For comparison, hard X-ray selected AGNs, [O III] bright AGNs (Heckman et al. 2005), optically selected Type 2 quasars (Ptak et al. 2006) and double-peaked [O III]-selected dual AGN sample of Liu et al. (2013) are shown in sky blue squares (Type 1s as filled and Type 2s as open), grey circles (Type 1s as filled and Type 2s as open), grey open upward triangles and yellow hourglasses, respectively. The mean relation for hard X-ray selected AGNs (both Type 1 and Type 2) and optically selected Type 1 AGNs (Heckman et al. 2005), optically selected Type 2 AGNs (Heckman et al. 2005) and double-peaked [O III]-selected dual AGNs (Liu et al. 2013) are shown in blue dashed-dotted-dotted, grey dashed and yellow dotted lines. Right panel: unabsorbed 2-10 keV luminosity vs. extinction-corrected [O III] luminosity. For comparison, nearby optically selected Seyfert galaxies (Panessa et al. 2006) are shown in grey circles. The grey dashed-dotted line is the mean relation for mixed Seyferts in nearby galaxies (Panessa et al. 2006) and the yellow dotted line is that for double-peaked [O III]-selected dual AGNs (Liu et al. 2013).

Table 4. X-ray Luminosity of the Five [O III]-Selected Dual AGN Targets.

Name	$\log L_{X,0.5-8}$	$\log L_{X,0.5-2}$	$\log L_{X,2-10}$	$\log L_{X,2-10,obs}$	$\log L_{[O III],obs}$	$\log L_{[O III],cor}$	SFR	$\log L_{SF,0.5-2}^{SF}$	$\log L_{SF,2-10}^{SF}$
(1)	(2)	(3)	(4)	(5)	(6)	(7)	(8)	(9)	(10)
J0907+5203a	$41.67^{+0.08}_{-0.06}$	$40.68^{+0.26}_{-0.16}$	$41.75^{+0.08}_{-0.07}$	$41.71^{+0.08}_{-0.07}$	$40.76^{+0.09}_{-0.11}$	$40.94^{+0.09}_{-0.11}$	$0.59^{+1.61}_{-0.52}$	$39.42^{+0.57}_{-0.94}$	$39.47^{+0.57}_{-0.94}$
J0907+5203b*	$42.35^{+0.04}_{-0.04}$	$41.89^{+0.10}_{-0.08}$	$42.27^{+0.05}_{-0.04}$	$42.20^{+0.05}_{-0.04}$	$40.66^{+0.04}_{-0.05}$	$40.98^{+0.04}_{-0.05}$	$1.28^{+2.95}_{-0.94}$	$39.76^{+0.52}_{-0.58}$	$39.81^{+0.52}_{-0.58}$
J0805+2818a	$42.24^{+0.09}_{-0.07}$	$41.92^{+0.12}_{-0.09}$	$42.01^{+0.15}_{-0.11}$	$41.97^{+0.15}_{-0.11}$	$42.27^{+0.03}_{-0.03}$	$42.53^{+0.03}_{-0.03}$	$11.68^{+15.90}_{-6.95}$	$40.72^{+0.37}_{-0.39}$	$40.77^{+0.37}_{-0.39}$
J0805+2818b	< 41.87	< 41.81	< 41.71	< 41.68	$41.25^{+0.11}_{-0.15}$	$41.25^{+0.11}_{-0.15}$	$2.24^{+3.31}_{-1.38}$	$40.00^{+0.39}_{-0.41}$	$40.05^{+0.39}_{-0.41}$
J1330-0036a	< 40.90	< 40.71	< 41.05	< 41.01	$40.29^{+0.02}_{-0.02}$	$40.45^{+0.02}_{-0.02}$	$0.35^{+0.49}_{-0.21}$	$39.20^{+0.38}_{-0.39}$	$39.24^{+0.38}_{-0.39}$
J1330-0036b	$41.16^{+0.13}_{-0.10}$	$40.84^{+0.18}_{-0.13}$	$40.96^{+0.21}_{-0.14}$	$40.92^{+0.21}_{-0.14}$	$40.92^{+0.09}_{-0.11}$	$41.21^{+0.09}_{-0.11}$	$3.98^{+6.69}_{-2.57}$	$40.25^{+0.43}_{-0.45}$	$40.30^{+0.43}_{-0.45}$
J1058+3144a	< 41.32	< 41.20	< 41.30	< 41.26	$40.50^{+0.05}_{-0.06}$	$40.51^{+0.05}_{-0.06}$	$1.95^{+2.73}_{-1.19}$	$39.94^{+0.38}_{-0.41}$	$39.99^{+0.38}_{-0.41}$
J1058+3144b*	$42.61^{+0.05}_{-0.05}$	$42.12^{+0.31}_{-0.18}$	$42.61^{+0.05}_{-0.05}$	$42.47^{+0.05}_{-0.05}$	$41.02^{+0.08}_{-0.09}$	$41.24^{+0.08}_{-0.09}$	$2.44^{+5.33}_{-1.75}$	$40.04^{+0.50}_{-0.55}$	$40.09^{+0.50}_{-0.55}$
J1544+0446a	$40.49^{+0.24}_{-0.15}$	$40.35^{+0.26}_{-0.16}$	< 40.81	< 40.77	$39.82^{+0.14}_{-0.20}$	$40.16^{+0.14}_{-0.20}$	$0.37^{+1.09}_{-0.34}$	$39.22^{+0.59}_{-1.07}$	$39.27^{+0.59}_{-1.07}$
J1544+0446b*	$41.87^{+0.06}_{-0.05}$	$41.43^{+0.21}_{-0.14}$	$41.75^{+0.07}_{-0.06}$	$41.63^{+0.07}_{-0.06}$	$40.08^{+0.11}_{-0.15}$	$40.42^{+0.11}_{-0.15}$	$0.91^{+2.27}_{-0.72}$	$39.61^{+0.54}_{-0.68}$	$39.66^{+0.54}_{-0.68}$

NOTE—(2)-(4) Unabsorbed luminosity in 0.5-8 (F), 0.5-2 (S) and 2-10 keV bands. The luminosity of targets with * are derived from the fitted spectrum, while the others are converted by assuming an absorbed power-law with a photon index of 1.7 and an absorption column density $N_H = 10^{22} \text{ cm}^{-2}$; (5) Observed luminosity in 2-10 keV bands; (6)-(7) Observed and extinction-corrected [O III] luminosity; (8) Fiber star formation rate in units of $M_\odot \text{ yr}^{-1}$ given by the MPA-JHU DR7 catalog inferred from $D_n(4000)$; (9)-(10) 0.5-2 (S) and 2-10 keV bands X-ray luminosities due to star formation.

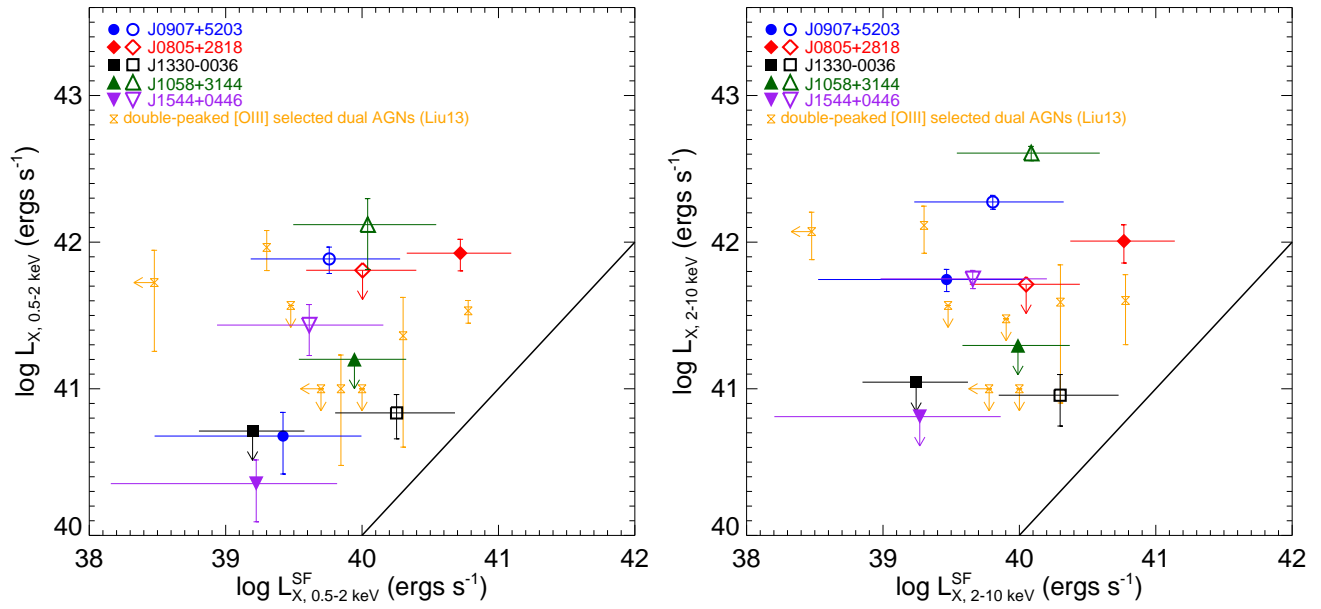


Figure 6. X-ray luminosities vs. the expected contribution from star-formation-related processes. Left panel for soft band and right panel for hard band. The solid line shows the equality relation. Also shown for comparison (in yellow hourglasses) are the double-peaked [O III]-selected dual AGN sample of Liu et al. (2013).

strong Balmer absorption features in the SDSS spectrum characteristic of post-starburst galaxies (Figure 7). For the NW nucleus, both the spatial profile of the X-ray source and the comparison between the observed to the expected star-formation-induced X-ray luminosities (Figure 6) are consistent with the AGN scenario. For the SE nucleus, on the other hand, the upper limits of the X-ray luminosities (Figure 6) are still consistent with the presence of an additional AGN, although the possibility that one AGN in the NW nucleus ionizes gas in both galaxies cannot be ruled out.

4.3.3. *SDSS J1330–0036*

The NW nucleus (J1330–0036a) in the merger is optically classified as an H II/AGN composite whereas the SE nucleus (J1330–0036b) a Type 2 Seyfert (Figure 3). Only the SE nucleus was detected in both soft and hard X-ray bands; the NW nucleus was not detected in either. The host galaxy of the NW nucleus shows strong Balmer absorption features in the SDSS spectrum characteristic of post-starburst galaxies (Figure 7). For the SE nucleus, the observed X-ray luminosities are similar to those expected from star-formation-induced X-ray luminosities (Figure 6), although an additional AGN component cannot be ruled out given significant uncertainties in the estimates. For the NW nucleus, on the other hand, the upper limits of the X-ray luminosities (Figure 6) are still consistent with the presence of an additional AGN, although the possibility that one AGN in the SE nucleus ionizes gas in both galaxies cannot be ruled out.

4.3.4. *SDSS J1058+3144*

The SW nucleus (J1058+3144a) in the merger is optically classified as an H II/AGN composite whereas the NE nucleus (J1058+3144b) a Type 2 Seyfert (Figure 3). Only the NE nucleus was detected in both soft and hard X-ray bands; the SW nucleus was not detected in either. The NE nucleus has enough counts for X-ray spectral analysis, which suggests moderate nuclear obscuration, with an estimated column density of $N_{\text{H}} \approx 6.4_{-4.5}^{+6.3} \times 10^{22} \text{ cm}^{-2}$. For the NE nucleus, both the spatial profile of the X-ray source and the comparison between the observed to the expected star-formation-induced X-ray luminosities (Figure 6) are consistent with the AGN scenario. For the SW nucleus, on the other hand, the upper limits of the X-ray luminosities (Figure 6) are still consistent with the presence of an additional AGN, although the possibility that one AGN in the NE nucleus ionizes gas in both galaxies cannot be ruled out.

4.3.5. *SDSS J1544+0446*

The SW nucleus (J1544+0446a) in the merger is optically classified as a LINER whereas the NE nucleus

(J1544+0446b) a LINER, Type 2 Seyfert or composite (Figure 3). The NE nucleus was detected in both soft and hard X-ray bands; the SW nucleus was detected only in the soft X-ray band. The NE nucleus has enough counts for X-ray spectral analysis, which suggests moderate nuclear obscuration, with an estimated column density of $N_{\text{H}} \approx 3.9_{-2.7}^{+3.2} \times 10^{22} \text{ cm}^{-2}$. For the NE nucleus, both the spatial profile of the X-ray source and the comparison between the observed to the expected star-formation-induced X-ray luminosities (Figure 6) are consistent with the AGN scenario. An additional AGN component is likely also for the SW nucleus because the observed soft X-ray luminosity is significantly larger than that expected from star-formation-related activity, despite significant uncertainties.

It is noteworthy that those target galaxies without X-ray detection tend to have a blue color in the composite SDSS image (Figure 2). These seem to be relatively small galaxies with young stellar populations. One possibility is that the X-ray emission from these galaxies is dominated by star formation and they are more likely to host a dwarf SMBH which is harder to detect. Whether this is a definitive trend can only be answered with a sizable sample of close pairs.

In summary, the new *Chandra* X-ray observations support the dual-AGN scenario for two of our five [O III]-selected targets (SDSS J0907+5203 and SDSS J1544+0446). For the other three targets (SDSS J0805+2818, SDSS J1330–0036, and SDSS J1058+3144), the existing data are still consistent with the dual-AGN scenario, although the possibility of only one AGN ionizing both components in the mergers cannot be ruled out.

5. DISCUSSION

5.1. *Systematically Smaller X-ray-to-[O III]-luminosity Ratio in Dual AGNs than in Single AGNs*

Figure 5 shows the relation between the hard X-ray luminosity and the [O III] luminosity for each nucleus in our targets. We compare the X-ray-to-[O III]-luminosity ratio of our new targets studied in this work to those observed in both single AGNs and dual AGNs systematically selected from double-peaked [O III] emission lines Liu et al. (2010a, see also Wang et al. 2009; Smith et al. 2010; Ge et al. 2012; Lyu & Liu 2016; Yuan et al. 2016). We examine both the relation between the observed hard X-ray luminosity $L_{X,2-10 \text{ keV,observed}}$ and the observed [O III] luminosity $L_{[\text{O III}],\text{observed}}$, and that between the unabsorbed hard X-ray luminosity $L_{X,2-10 \text{ keV,unabsorbed}}$ and the extinction-corrected [O III] luminosity $L_{[\text{O III}],\text{extinction-corrected}}$. We use the appro-

appropriate comparison samples for the two cases separately, because usually either the observed or the corrected luminosity is available in any given literature sample.

For the $L_{X,2-10\text{keV,observed}}-L_{[\text{O III}],\text{observed}}$ relation (left panel of Figure 5), the comparison samples include 47 hard X-ray (3–20 keV) selected local AGNs and 55 optically selected local [O III]-bright AGNs (Xu et al. 1999; Whittle 1992) studied by Heckman et al. (2005), and 8 optically selected Type 2 quasars from Ptak et al. (2006) at redshifts $z\sim 0.3-0.8$. Heckman et al. (2005) showed that single, optically selected Type 2 AGNs (the grey dashed line) have systematically lower $L_{X,2-10\text{keV,observed}}$ (by an average of 1.0 dex) at a given $L_{[\text{O III}],\text{observed}}$ than hard X-ray selected AGNs (both Type 1 and Type 2) and optically selected Type 1 AGNs (the blue dashed-dotted-dotted line), as expected for heavily absorbed AGNs (see also Mulchaey et al. 1994; Panessa et al. 2006). Liu et al. (2013) has shown that the four dual AGNs (individually as the yellow standing glasses and collectively as the yellow dotted line) selected from the parent sample of Type 2 AGNs with double-peaked [O III] emission lines (Liu et al. 2010b) have systematically smaller $L_X/L_{[\text{O III}]}$ (observed) ratios (by $\sim 0.8 \pm 0.2$ dex on average) than even optically selected single Type 2 AGNs. Our new targets seem to have X-ray-to-[O III]-luminosity ratios that are on average in between that observed in single, optically selected Type 2 AGNs and that observed in the dual AGNs selected from double-peaked [O III] emission lines (with some ambiguities and uncertainties due to the upper limits of several measurements).

A similar trend is also seen in the $L_{X,2-10\text{keV,unabsorbed}}-L_{[\text{O III}],\text{extinction-corrected}}$ relation as shown in the right panel of Figure 5). Again, our new targets seem to have X-ray-to-[O III]-luminosity ratios that are on average in between that observed in single AGNs (the grey dashed-dotted line) and that observed in dual AGNs selected from double-peaked [O III] emission lines (the yellow dotted line). The comparison sample of single AGNs includes 47 Palomar Seyfert galaxies (optically selected Type 1 and Type 2 Seyferts drawn from the Palomar survey of nearby galaxies by Ho et al. 1995) from Panessa et al. (2006). Panessa et al. (2006) has demonstrated that after properly accounting for absorption correction (including for Compton-thick sources), optically selected Type 1 and Type 2 Seyferts follow the same $L_{X,2-10\text{keV,unabsorbed}}-L_{[\text{O III}],\text{extinction-corrected}}$ relation. In particular, optically selected Type 2 Seyferts, which were significantly X-ray weaker than Type 1 Seyferts, also obey the same relation, after the ‘‘Compton thick’’ luminosity correction. Liu et al. (2013) has shown that after correction for gas absorption and dust

extinction, the unabsorbed hard X-ray luminosities of double-peaked-[O III]-selected dual AGNs appear to be $\sim 2.4 \pm 0.3$ dex smaller (at $\log L_{[\text{O III}]}$ of 42.0) than those expected from the Panessa et al. (2006) relation, $\log L_X = 1.22 \log L_{[\text{O III}]} - 7.34$, although the absorption correction of dual AGNs may have been significantly underestimated.

5.2. Interpretation: Enhanced Nuclear Absorption from Merger-induced Gas Inflows

Liu et al. (2013) has suggested that the observed X-ray weak tendency in dual AGNs selected in Type 2 AGNs with double-peaked narrow [O III] lines is caused by a combination of a higher nuclear gas column, which may be induced by merger events, and an orientation bias related to the double-peak narrow emission-line selection. In contrast to the Liu et al. (2013) sample, our targets are not subject to the orientation bias due to the line-of-sight velocity splitting requirement caused by the double-peaked [O III] selection. On the other hand, our sample is likely to have a higher nuclear absorption from merger-induced gas inflows than that in single local AGNs, similar to the case of double-peaked-[O III]-selected dual AGNs. Arising from the narrow-line regions that are much further out, the [O III] emission is less subject to nuclear gas absorption and dust obscuration than the hard X-ray emission from the black hole accretion disk corona, which would explain the systematically smaller hard-X-ray-to-[O III]-luminosity ratios observed in dual than in single AGNs. The fact that our targets seem to have hard-X-ray-to-[O III]-luminosity ratios that are smaller than that seen in single AGNs but larger than that observed in double-peaked-[O III]-selected dual AGNs is consistent with the conclusion of Liu et al. (2013) that a combination of two effects (i.e., both merger-enhanced absorption and obscuration and an orientation selection bias) are at work for double-peaked-[O III]-selected dual AGNs.

6. CONCLUSIONS

Dual AGNs are crucial to our understanding of the accretion and dynamical evolution of SMBHs in mergers, the effects of merger-induced activity on galaxy evolution, and the initial conditions of close binary SMBHs. Building on *Chandra*’s previous success on its unique power in resolving dual AGNs, here we have studied the X-ray properties of a sample of five optically selected dual AGN candidates. Our targets were drawn from a sample of 1286 [O III]-selected AGN pairs (both Type 1 and Type 2 sources) systematically selected from the SDSS DR7. Each of the targets contains two nuclei separated by 3–9 kpc in projection, both of which are optically classified as Type 2 (obscured) AGNs based on

diagnostic ratios of the optical narrow emission lines. While being systematically selected from the largest sample of dual AGN candidates, the optical classification was inconclusive. Furthermore, because the double nuclei are close (with physical projected separations of a few kpc), there may be only one AGN ionizing both galaxies, producing two optical emission-line nuclei. Arguments based on the spatial distribution of ionization parameters estimated from optical emission lines cannot conclusively discriminate between the single- and dual-AGN scenarios (e.g., Liu et al. 2010b). The new *Chandra* ACIS-S X-ray imaging presented here helps solve the problem by resolving and localizing the ionizing sources directly in the X-rays. The X-ray confirmation of a systematically selected sample also helps place the optically inferred dual-AGN frequency on a firmer ground (Liu et al. 2011). Our main findings are summarized as the following:

- *Chandra*'s superb spatial resolution and sensitivity in the X-rays allowed us to localize the ionizing sources and determine their X-ray properties. Seven of the ten nuclei were detected in the full 0.5–8 keV band. Six were detected in both soft (0.5–2 keV) and hard (2–8 keV) bands, whereas one nucleus was detected in the soft band only. Three nuclei were undetected in the X-rays (Table 3).
- The hard X-rays directly probe the accretion disk corona of the accreting SMBHs, providing a more robust estimate of the intrinsic AGN luminosity than using [O III] λ 5007 luminosity as a surrogate. In three of the ten nuclei we observed enough counts to perform spectral fittings to constrain the X-ray spectral properties and absorption column densities. We fit each X-ray spectrum with an absorbed power-law model. The best-fit power-law spectral indices and the absorption column densities are consistent with them being Type 2 AGNs for all three nuclei. For the other four X-ray detected nuclei, we have estimated their spectral properties and luminosities using hardness ratios. For the three sources without X-ray detection, we estimate the X-ray net counts 3σ upper limit using the CIAO tool *aprate* (Section 3.2).
- Combined with independent star formation rate estimates empirically calibrated based on the host-galaxy stellar continua, the new *Chandra* X-ray observations allowed us to evaluate the dual-AGN hypothesis for each target. We have confirmed two (SDSS J0907+5203 and SDSS J1544+0446) of the five targets as bona-fide dual AGNs. For the other three targets, the existing data are consistent with the dual-AGN scenario, but we cannot conclusively rule out the possibility of stellar and/or shock heating and/or one AGN ionizing both gaseous components in a merger (Section 4.3).
- The average X-ray-to-[O III] luminosity ratio in our targets seems to be systematically smaller than that observed in single AGNs but is higher than that seen in dual AGNs selected from AGNs with double-peaked narrow emission lines. We suggest that the systematically smaller X-ray-to-[O III] luminosity ratio observed in dual AGNs than in single AGNs is due to a high nuclear gas column likely from strong merger-induced inflows. Unlike double-peaked-[O III]-selected dual AGNs, the new sample selected from resolved galaxy pairs are not subject to the orientation bias caused by the double-peak line-of-sight velocity splitting selection, which also contributes to lowering the X-ray-to-[O III] luminosity ratio (Figure 5).

Our sample size is still too small for a statistical analysis to compare with theoretical predictions from simulations in a meaningful way (e.g., Capelo et al. 2017; Blecha et al. 2018; Rosas-Guevara et al. 2019; Solanes et al. 2019). To put the conclusions on a firm statistical ground, future wide-field, high-resolution, and high-sensitivity X-ray telescopes (such as Lynx X-ray Surveyor; The Lynx Team 2018) may detect thousands of dual AGNs, which will be needed to fully understand black hole growth in mergers and dual AGNs (e.g., Burke-Spolaor et al. 2018; Koss et al. 2019).

ACKNOWLEDGEMENTS

We thank M. Strauss for his generous support and guidance on the project. M.H. and Z.L. acknowledge support by the National Key Research and Development Program of China (2017YFA0402703). X.L. and H.G. acknowledge support by NASA through *Chandra* Award Number GO3-14103X issued by the *Chandra* X-ray Observatory Center, which is operated by the Smithsonian Astrophysical Observatory for and on behalf of NASA under contract NAS 8-03060. Y.S. acknowledges support from the Alfred P. Sloan Foundation and NSF grant 1715579.

This research has made use of software provided by the *Chandra* X-ray Center in the application packages CIAO, ChIPS, and Sherpa.

Funding for the Sloan Digital Sky Survey IV has been provided by the Alfred P. Sloan Foundation, the U.S.

Department of Energy Office of Science, and the Participating Institutions. SDSS-IV acknowledges support and resources from the Center for High-Performance Computing at the University of Utah. The SDSS website is www.sdss.org.

SDSS-IV is managed by the Astrophysical Research Consortium for the Participating Institutions of the SDSS Collaboration including the Brazilian Participation Group, the Carnegie Institution for Science, Carnegie Mellon University, the Chilean Participation Group, the French Participation Group, Harvard-Smithsonian Center for Astrophysics, Instituto de Astrofísica de Canarias, The Johns Hopkins University, Kavli Institute for the Physics and Mathematics of the Universe (IPMU) / University of Tokyo, Lawrence Berkeley National Laboratory, Leibniz Institut für Astrophysik Potsdam (AIP), Max-Planck-Institut für Astronomie (MPIA Heidelberg), Max-Planck-Institut für Astrophysik (MPA Garching), Max-Planck-Institut für Extraterrestrische Physik (MPE), National Astronomical Observatories of China, New Mexico State University, New York University, University of Notre Dame, Observatório Nacional / MCTI, The Ohio State University, Pennsylvania State University, Shanghai As-

tronomical Observatory, United Kingdom Participation Group, Universidad Nacional Autónoma de México, University of Arizona, University of Colorado Boulder, University of Oxford, University of Portsmouth, University of Utah, University of Virginia, University of Washington, University of Wisconsin, Vanderbilt University, and Yale University.

Facilities: *Chandra* X-ray Observatory (ACIS), Sloan

APPENDIX

In this appendix, we present details of our spectral fitting analysis to carefully measure the host-galaxy stellar continuum and to model the emission-line fluxes over the host-subtracted spectrum. For the host galaxy spectral fitting, we adopt the penalized Pixel-Fitting (pPXF) method² (Cappellari & Emsellem 2004). The method works directly in the pixel space and uses the maximum penalized likelihood formalism to extract as much information as possible from the spectra while suppressing the noise in the solution. After subtracting the host-galaxy continuum using the pPXF best-fit solution, we then model the emission-line-only spectrum using the spectral fitting code *qsofit*³ (Shen et al. 2018). Figures 7 and 8 show the fitting results for all the 10 nuclei in our targets.

REFERENCES

- Abazajian, K. N., Adelman-McCarthy, J. K., Agüeros, M. A., et al. 2009, *ApJS*, 182, 543
- Abbott, B. P., Abbott, R., Abbott, T. D., et al. 2016, *Phys. Rev. Lett.*, 116, 061102
- Amaro-Seoane, P., Audley, H., Babak, S., et al. 2017, *ArXiv e-prints* 1702.00786, [arXiv:1702.00786](https://arxiv.org/abs/1702.00786)
- Arzoumanian, Z., Baker, P. T., Brazier, A., et al. 2018, *ApJ*, 859, 47
- Baldwin, J. A., Phillips, M. M., & Terlevich, R. 1981, *PASP*, 93, 5
- Ballo, L., Braitto, V., Della Ceca, R., et al. 2004, *ApJ*, 600, 634
- Bassani, L., Dadina, M., Maiolino, R., et al. 1999, *ApJS*, 121, 473
- Bhowmick, A. K., Di Matteo, T., & Myers, A. D. 2019, *arXiv e-prints* 1902.05954, [arXiv:1902.05954](https://arxiv.org/abs/1902.05954)
- Bianchi, S., Chiaberge, M., Piconcelli, E., Guainazzi, M., & Matt, G. 2008, *MNRAS*, 386, 105
- Blecha, L., Snyder, G. F., Satyapal, S., & Ellison, S. L. 2018, *MNRAS*, 478, 3056
- Brassington, N. J., Ponman, T. J., & Read, A. M. 2007, *MNRAS*, 377, 1439
- Brinchmann, J., Charlot, S., White, S. D. M., et al. 2004, *MNRAS*, 351, 1151
- Burke-Spolaor, S., Blecha, L., Bogdanović, T., et al. 2018, in *Astronomical Society of the Pacific Conference Series*, Vol. 517, *Science with a Next Generation Very Large Array*, ed. E. Murphy, 677
- Capelo, P. R., Dotti, M., Volonteri, M., et al. 2017, *MNRAS*, 469, 4437
- Cappellari, M., & Emsellem, E. 2004, *PASP*, 116, 138
- Cash, W. 1979, *ApJ*, 228, 939
- Centrella, J., Baker, J. G., Kelly, B. J., & van Meter, J. R. 2010, *Reviews of Modern Physics*, 82, 3069
- Colpi, M., & Dotti, M. 2011, *Advanced Science Letters*, 4, 181
- Comerford, J. M., Pooley, D., Barrows, R. S., et al. 2015, *ApJ*, 806, 219
- Comerford, J. M., Gerke, B. F., Newman, J. A., et al. 2009, *ApJ*, 698, 956
- Cornish, N., & Robson, T. 2018, *ArXiv e-prints* 1803.01944, [arXiv:1803.01944](https://arxiv.org/abs/1803.01944)

² <https://pypi.org/project/ppxf/>

³ <https://github.com/legolason/PyQSOFit>

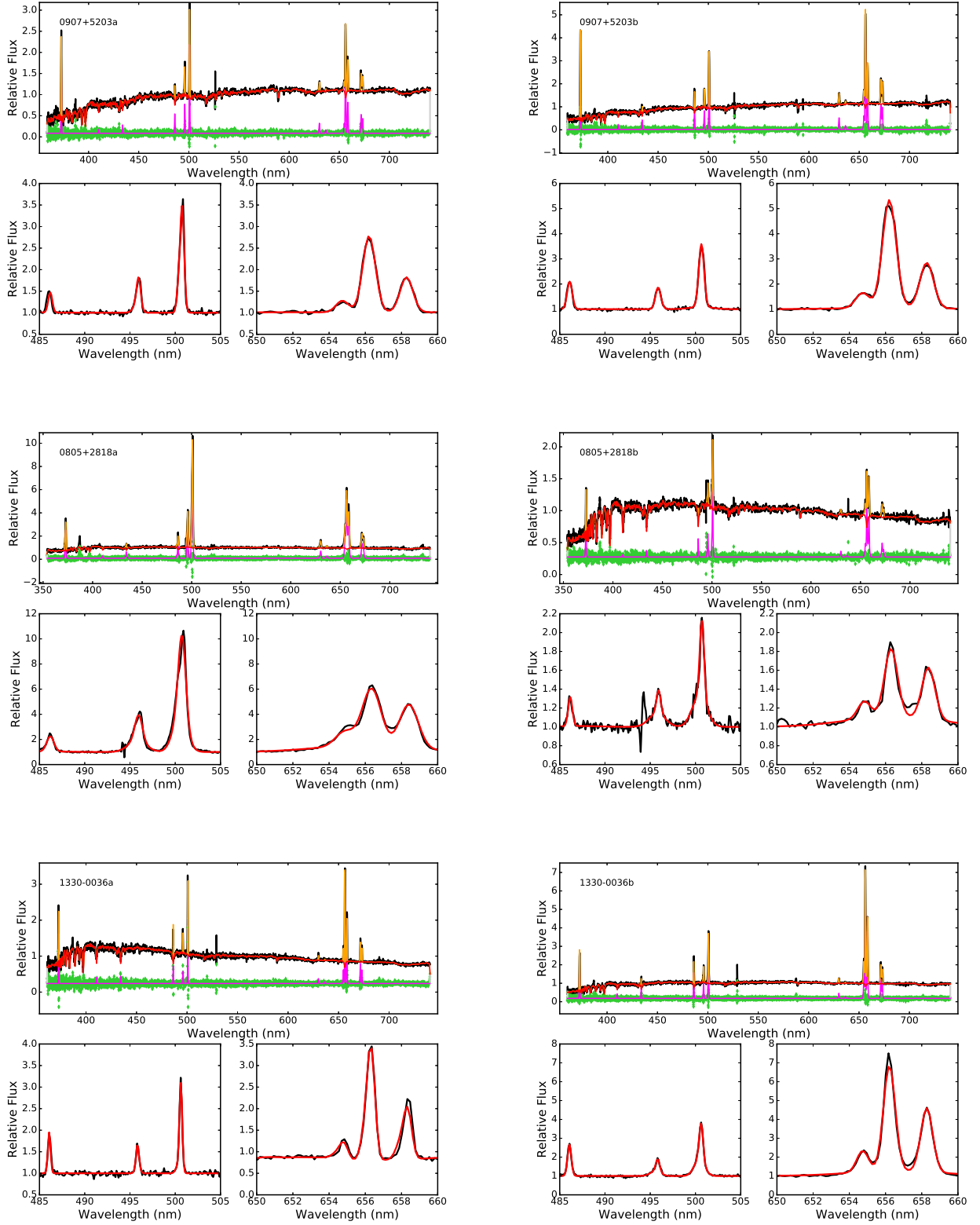


Figure 7. Spectral fitting results for the two nuclei in J0907+5203, J0805+2818 and J1330-0036 from top to bottom. For each nucleus, the upper panel shows the best-fit model from the pPXF fit for the host-galaxy stellar continuum shown in red overlaid on top of the SDSS spectrum shown in black. Also shown are the host-galaxy-subtracted emission-line spectrum in magenta, the total model (i.e., host+emission line) in orange, and the total residual (i.e., data-model) in green. The bottom panels show the best-fit model (in red) for the host-subtracted emission lines from the qsofit analysis overlaid on top of the data (in black).

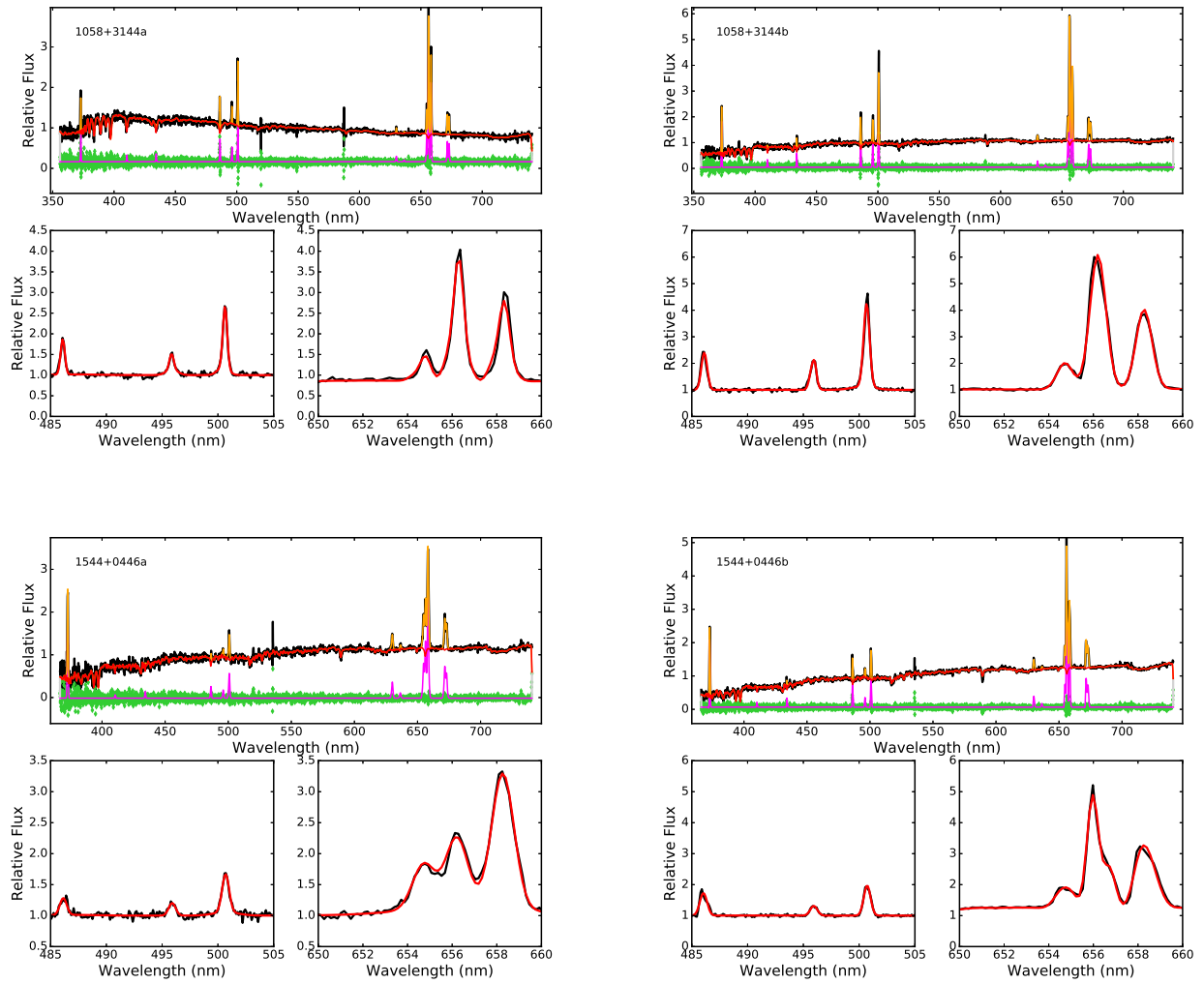


Figure 8. Same as Figure 7, but for J1058+3144 and J1544+0446.

- De Rosa, A., Vignali, C., Husemann, B., et al. 2018, *MNRAS*, 480, 1639
- Ellison, S. L., Secrest, N. J., Mendel, J. T., Satyapal, S., & Simard, L. 2017, *MNRAS*, 470, L49
- Fabbiano, G., Wang, J., Elvis, M., & Risaliti, G. 2011, *Nature*, 477, 431
- Ferrarese, L., & Ford, H. 2005, *SSRv*, 116, 523
- Fu, H., Wrobel, J. M., Myers, A. D., Djorgovski, S. G., & Yan, L. 2015, *ApJL*, 815, L6
- Fu, H., Steffen, J. L., Gross, A. C., et al. 2018, *ArXiv e-prints* 1801.00792, arXiv:1801.00792
- Gatti, M., Shankar, F., Bouillot, V., et al. 2016, *MNRAS*, 456, 1073
- Ge, J.-Q., Hu, C., Wang, J.-M., Bai, J.-M., & Zhang, S. 2012, *ApJS*, 201, 31
- Gerke, B. F., Newman, J. A., Lotz, J., et al. 2007, *ApJL*, 660, L23
- Gilfanov, M. 2004, *MNRAS*, 349, 146
- Green, P. J., Myers, A. D., Barkhouse, W. A., et al. 2010, *ApJ*, 710, 1578
- Green, P. J., Aldcroft, T. L., Richards, G. T., et al. 2009, *ApJ*, 690, 644
- Grimm, H.-J., Gilfanov, M., & Sunyaev, R. 2003, *MNRAS*, 339, 793
- Guainazzi, M., Matt, G., Antonelli, L. A., et al. 1999, *MNRAS*, 310, 10
- Gültekin, K., Richstone, D. O., Gebhardt, K., et al. 2009, *ApJ*, 698, 198
- Heckman, T. M., Ptak, A., Hornschemeier, A., & Kauffmann, G. 2005, *ApJ*, 634, 161
- Ho, L. C., Filippenko, A. V., & Sargent, W. L. 1995, *ApJS*, 98, 477
- Hou, M., Li, Z., Peng, E. W., & Liu, C. 2017, *ApJ*, 846, 126
- Hudson, D. S., Reiprich, T. H., Clarke, T. E., & Sarazin, C. L. 2006, *A&A*, 453, 433
- Hughes, S. A. 2009, *ARA&A*, 47, 107
- Kauffmann, G., & Heckman, T. M. 2009, *MNRAS*, 397, 135
- Kauffmann, G., Heckman, T. M., White, S. D. M., et al. 2003a, *MNRAS*, 341, 33
- Kauffmann, G., Heckman, T. M., Tremonti, C., et al. 2003b, *MNRAS*, 346, 1055
- Kewley, L. J., Dopita, M. A., Sutherland, R. S., Heisler, C. A., & Trevena, J. 2001, *ApJ*, 556, 121
- Kewley, L. J., Geller, M. J., & Barton, E. J. 2006, *AJ*, 131, 2004
- Kocevski, D. D., Brightman, M., Nandra, K., et al. 2015, *ApJ*, 814, 104
- Komossa, S., Burwitz, V., Hasinger, G., et al. 2003, *ApJL*, 582, L15
- Kormendy, J., & Richstone, D. 1995, *ARA&A*, 33, 581
- Koss, M., Mushotzky, R., Treister, E., et al. 2011, *ApJL*, 735, L42
- Koss, M., U, V., Hodges-Kluck, E., et al. 2019, *arXiv e-prints* 1903.06720, arXiv:1903.06720
- Koss, M. J., Glidden, A., Baloković, M., et al. 2016, *ApJL*, 824, L4
- LaMassa, S. M., Heckman, T. M., Ptak, A., et al. 2011, *ApJ*, 729, 52
- Lansbury, G. B., Gandhi, P., Alexander, D. M., et al. 2015, *ApJ*, 809, 115
- Lehmer, B. D., Alexander, D. M., Bauer, F. E., et al. 2010, *ApJ*, 724, 559
- Liu, X., Civano, F., Shen, Y., et al. 2013, *ApJ*, 762, 110
- Liu, X., Greene, J. E., Shen, Y., & Strauss, M. A. 2010a, *ApJL*, 715, L30
- Liu, X., Lazio, T. J. W., Shen, Y., & Strauss, M. A. 2018, *ApJ*, 854, 169
- Liu, X., Shen, Y., Strauss, M. A., & Greene, J. E. 2010b, *ApJ*, 708, 427
- Liu, X., Shen, Y., Strauss, M. A., & Hao, L. 2011, *ApJ*, 737, 101
- Lyu, Y., & Liu, X. 2016, *MNRAS*, 463, 24
- Matt, G., Guainazzi, M., Frontera, F., et al. 1997, *A&A*, 325, L13
- Mazzarella, J. M., Iwasawa, K., Vavilkin, T., et al. 2012, *AJ*, 144, 125
- Mulchaey, J. S., Koratkar, A., Ward, M. J., et al. 1994, *ApJ*, 436, 586
- Nardini, E. 2017, *MNRAS*, 471, 3483
- Oke, J. B. 1974, *ApJS*, 27, 21
- Panessa, F., Bassani, L., Cappi, M., et al. 2006, *A&A*, 455, 173
- Park, T., Kashyap, V. L., Siemiginowska, A., et al. 2006, *ApJ*, 652, 610
- Pfeifle, R. W., Satyapal, S., Secrest, N. J., et al. 2019, *arXiv e-prints* 1904.10955, arXiv:1904.10955
- Ptak, A., Heckman, T., Levenson, N. A., Weaver, K., & Strickland, D. 2003, *ApJ*, 592, 782
- Ptak, A., Zakamska, N. L., Strauss, M. A., et al. 2006, *ApJ*, 637, 147
- Ranalli, P., Comastri, A., & Setti, G. 2003, *A&A*, 399, 39
- Risaliti, G., Maiolino, R., & Salvati, M. 1999, *ApJ*, 522, 157
- Rosas-Guevara, Y. M., Bower, R. G., McAlpine, S., Bonoli, S., & Tissera, P. B. 2019, *MNRAS*, 483, 2712
- Salim, S., Rich, R. M., Charlot, S., et al. 2007, *ApJS*, 173, 267
- Satyapal, S., Secrest, N. J., Ricci, C., et al. 2017, *ApJ*, 848, 126
- Shen, Y., Hall, P. B., Horne, K., et al. 2018, *ArXiv e-prints* 1810.01447, arXiv:1810.01447

- Smith, K. L., Shields, G. A., Bonning, E. W., et al. 2010, *ApJ*, 716, 866
- Solanes, J. M., Perea, J. D., Valentí-Rojas, G., et al. 2019, *A&A*, 624, A86
- Teng, S. H., Schawinski, K., Urry, C. M., et al. 2012, *ApJ*, 753, 165
- The Lynx Team. 2018, arXiv e-prints 1809.09642, arXiv:1809.09642
- Treister, E., Privon, G. C., Sartori, L. F., et al. 2018, *ApJ*, 854, 83
- Turner, T. J., George, I. M., Nandra, K., & Mushotzky, R. F. 1997a, *ApJS*, 113, 23
- . 1997b, *ApJ*, 488, 164
- Veilleux, S., & Osterbrock, D. E. 1987, *ApJS*, 63, 295
- Vignali, C., Piconcelli, E., Perna, M., et al. 2018, *MNRAS*, 477, 780
- Vignati, P., Molendi, S., Matt, G., et al. 1999, *A&A*, 349, L57
- Wang, J., Chen, Y., Hu, C., et al. 2009, *ApJL*, 705, L76
- Wang, Q. D. 2004, *ApJ*, 612, 159
- Whittle, M. 1992, *ApJS*, 79, 49
- Xu, C., Livio, M., & Baum, S. 1999, *AJ*, 118, 1169
- Xu, D., & Komossa, S. 2009, *ApJL*, 705, L20
- Yuan, S., Strauss, M. A., & Zakamska, N. L. 2016, *MNRAS*, 462, 1603
- Zezas, A., Alonso-Herrero, A., & Ward, M. J. 2001, *Ap&SS*, 276, 601